

Topology optimization for additive manufacturing: accounting for overhang limitations using a virtual skeleton

Yoram Mass^{a,*}, Oded Amir^a

^a*Faculty of Civil Engineering, Technion - Israel Institute of Technology
Technion City, Haifa 3200003, Israel*

Abstract

This article proposes a new method for reducing the amount of support material required for 3-D printing of complex designs generated by topology optimization. This procedure relies on solving sequentially two structural optimization problems – the first on a discrete truss-based model and the second on a continuum-based model. In the optimization of the discrete model, the maximum overhang limitation is imposed based on geometrical parameters. The optimized discrete pattern is then projected on to the continuum so that it influences the material distribution in the continuum optimization. The method is explained and investigated on a set of test cases in 2-D and subsequently demonstrated on examples in 3-D. Numerical results indicate that the designs obtained by this approach exhibit improved printability as they have fewer overhanging features. In some cases, practically no supporting material will be required for printing the optimized design.

Keywords: Additive manufacturing, topology optimization, 3-D printing, overhang angles

1. Introduction

Topology optimization is a computational approach for optimizing the distribution of material in a given design domain, such that a certain objective is minimized subject to design and response constraints. Extensive reviews of various formulations and implementation techniques can be found in the monograph [1] and in recent review articles [2, 3]. Even though topology optimization was intended initially for optimizing load-bearing structures, it is currently applied in various engineering and science fields, would it be buildings, aircraft, automotive, acoustics, photonics, fluid motion, heat transfer and medicine, among others [1, 4, 5, 6, 7]. Due to the complexity of the resulting layouts, the question of how to build such designs was asked, and partly answered. The fact that machining was one of the most powerful manufacturing tools for a long time led researchers to look into this direction [8, 9]. Nowadays, the increasing availability of Additive Manufacturing (AM) can be a game changer as it opens up new opportunities for exploiting the full potential of topology optimization procedures as a means of generating complex, highly optimized designs.

Even though the first patent was recorded 30 years ago by Hull [10], AM technologies have been available on the market for only a few years. From then on, they have been implemented in many fields because of their versatility,

*Corresponding author

Email address: yoram.mass@technion.ac.il (Yoram Mass)

reliability and the constant improvement and use of new materials [11]. Different types of plastics, resins, metals, and even concrete are currently available as base materials [12, 13, 14], whereas each particular AM technology can fit one or several specific materials [15]. The current study focuses on a specific family of AM technologies, typically known as 3-D printing, which does not suffer from the same limitations as traditional manufacturing techniques [16], making it a better partner to topology optimization.

Even though AM technologies appear as very suitable for fabricating complex shapes generated by topology optimization, they still suffer from a common limitation: they are unable to print overhanging patterns. Investigations were carried out to evaluate the maximal angle which depends on the specific technology and material. As input in this work, without loss of generality of the approach, ~~we will assume it will be assumed~~ that the limit is ~~approximately~~ 45° [17]. This limitation implies that there are still design features that cannot be fabricated accurately without using temporary supports or scaffolds. This poses a challenge for integrating topology optimization and AM, as it constrains the geometry that can be printed without extra cost – resulting from sacrificing support material and investing time in removing the supports after fabrication. Consequently, there is a clear motivation to develop new topology optimization approaches that can automatically account for such overhang limitations.

In one of the earliest contributions on topology optimization for AM, a procedure intended to locate the unprintable patterns was presented by Brackett et al. [18]. The method identifies the problematic areas by locating the boundaries of the cavities in the optimized design and checking which ones face downwards. Then, their orientations are compared to the allowable one. The components needing support are thus identified and the authors propose to fill the corresponding cavities with printable supporting lattice patterns. Several other fashions of addressing the problem were later suggested. Leary et al. [19] propose a method that modifies the theoretically optimal topology into a support-free one. To do so, supporting material is added in a printable manner, according to the maximum overhang angle, making it part of the structure. The lack of reanalysis after the operations unfortunately does not allow to determine the volume of added material, while the stiffness obviously must have increased because of this supplementary volume. While the above mentioned contributions deal essentially with the post-processing of a topological design that was generated by standard procedures, several recent studies proposed to embed the overhang limitation into the optimization process by either filtering or projection schemes. In the work by Gaynor and Guest [20, 21], intermediate variables are added as transition between design variables and physical ones, which is the classical scheme. For each element, the algorithm scans how this latter is supported, projecting the datum to the intermediate variable. If the material is not adequately supported, then its existence is forbidden. A similar approach has been proposed by Langelaar [22, 23], who developed a filter that mimics the AM process. He showed in his articles that not only this filter has the possibility to modify the geometry in order to create internal supports like in Gaynor’s works, but it can also produce external support from a completely unsupported pattern. A recent study from Qian [24] uses a formulation of the edge detection operators to control the undercut and the minimal overhang angle. A grayness constraint needs to be added to avoid boundary oscillations and to control topology. The target of his research is to propose a new method for reducing supporting structure without a motivation regarding compliance.

The work presented in this publication has the same goal as pursued in [20, 21, 22, 23] but is based on a different concept: ~~we suggest~~ ~~it is suggested~~ to use truss optimization – i.e. finding optimal structural layouts represented by discrete lines – as a means of imposing the allowable geometry according to the overhang limitation. The proposed approach consists of two sequential optimization steps. In the first step, truss optimization is performed based on a well-established formulation that finds the stiffest design subject to a volume constraint. This step begins with creating a collection of available truss bars, also known as the “ground structure”. According to the printing direction and the specific overhang limitation, the ground structure will include only printable bars that comply with the overhang limitation. The result of the first step is an optimal layout where each bar has its optimal cross-section area, and bars that have a negligible cross-section area are removed. In the second step, continuum topology optimization is performed based on the well-established density-based approach, again aiming to generate the stiffest design subject to a volume constraint. At this stage, the optimal truss does not serve as a load-bearing structure anymore, but only as a “virtual skeleton” upon which the continuum topology is built. A raster representation of the optimal truss is computed, which influences the elements in the design space of the continuum topology optimization through local enhancement of the stiffness, represented by Young’s modulus E . In other words, during the continuum topology optimization, ~~we give~~ ~~priority~~ ~~is given~~ to the spatial locations occupied by optimal truss bars. As a result, the continuum optimization tends to push material towards the location of the optimal truss, hence it can satisfy the overhang constraint without imposing it explicitly – allowing for convergence towards a printable continuum structure.

It is worth noting that the coupling between truss and continuum optimization has been utilized in other contexts, and these contributions have inspired the current work. Hybrid truss-continuum representations have been studied in the context of reinforced concrete, for force visualization [25] and for topological design [26]. In the latter, the continuum material is forced to wrap the discrete bars using a specialized filter. Another related approach was proposed by Norato et al. [27] and by Zhang et al. [28], where the location and sizes of discrete objects are optimized and then projected onto the continuum domain. This enables to incorporate various geometric constraints which are difficult to impose in standard density-based continuum approaches – as suggested also in this article. Although the authors do not relate their method to additive manufacturing, this approach can be interesting for 3-D printing because if only bars are used then closed voids cannot appear in the design, alleviating difficulties associated with removing powder and scaffolds.

The remainder of the article is organized as follows. The problem formulation is stated in detail in the Section 2, where details regarding both truss and continuum optimizations as well as about the coupling between them are provided. Demonstrative numerical examples in 2-D are presented in Section 3 followed by an analysis of the influence of the main parameters in Section 4. Finally, 3-D implementation is addressed in Section 5 and a concluding discussion is given in Section 6.

2. Problem statement

The most common problem formulation in topology optimization of load-bearing structures, since the pioneering publication of Bendsøe and Kikuchi [29], is the search for minimum compliance (or maximum stiffness) under a volume constraint. This formulation is the one used also in this work, both for the truss and the continuum optimization. The truss minimum compliance is stated based on the classical elastic design problem, see [1] and references therein. The continuum structure compliance is minimized following a density-based approach, in which finite elements are used, each one possessing a specific density ρ which serves as the design variable [30].

In order to compare the designs obtained in the current study with established results, the continuum problem is solved also with the 88-line code [31], which computes optimized designs with a density-based approach, but without considering the AM limitations. This latter reference layout and compliance allows us to evaluate the effectiveness of the proposed procedure as well as to compute the performance drop due to the added constraints.

In this section, the formulations used for the two optimization steps as well as the particularities of the \mathbf{T} matrix – the raster representation of the optimal truss – are presented. For the purpose of clarity, the overall process used in this study is depicted in Figure 1.

2.1. Truss optimization

2.1.1. Problem formulation

In AM technologies, the parts are printed inside a work volume. For Selective LASER Melting (SLM) for example, this volume is the internal void of the machine cubicle, filled with a powder bed. Thus, as long as the part lays inside these dimensions, it is possible to print it – possibly with the help of supports.

Following the computational layout optimization works developed by Dorn et al. [32] and augmented afterwards (see for example [1, 33] and references therein), the truss optimization problem is defined as a minimization of the compliance. An admissible ground structure is created where the truss elements' cross-section areas are optimized. It can be expressed by the matrix-vector notation as follows:

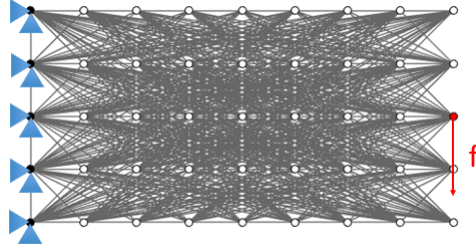
$$\begin{cases} \min_{\boldsymbol{\phi}} f = \mathbf{f}^T \mathbf{u}_1 \\ \text{s.t.} \begin{cases} g = \sum_{i=1}^{nbars} \phi_i l_i A_i - V^* \leq 0 \\ \phi_i \geq 0 \quad i = 1 \dots nbars \end{cases} \\ \text{with: } \mathbf{K} \mathbf{u}_1 = \mathbf{f} \end{cases} \quad (1)$$

where $\boldsymbol{\phi}$ is the vector of design variables, one for each truss bar; \mathbf{f} is the applied force; \mathbf{u}_1 is the nodal displacements vector; l_i and A_i are the length and the cross-section area of the i -th bar, respectively; V^* is the maximal allowed total volume; and \mathbf{K} is the stiffness matrix, computed as $\mathbf{K} = \sum_{i=1}^{nbars} \phi_i \frac{A_i E_i}{l_i} \mathbf{k}_i$ where \mathbf{k}_i encloses only geometric properties of the i -th bar and does not depend on the design variable.

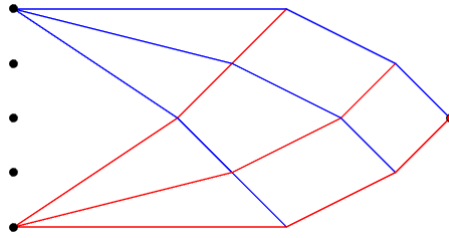
Considering the truss role, it is useful to ensure that a reasonable change in the parameters – except the printing direction – does not change significantly the truss structure. As the truss has eventually no mechanical role, defining



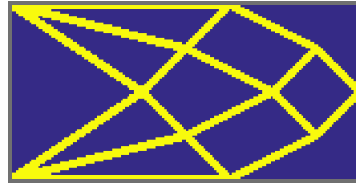
(a) Cantilever model



(b) Cleaned ground structure



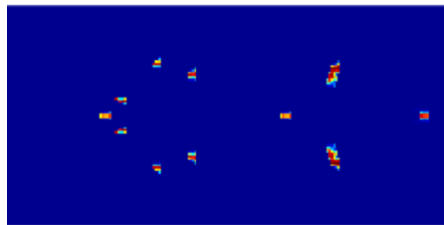
(c) Resulting optimal truss



(d) Truss raster representation



(e) Resulting optimal continuum structure



(f) Remaining unprintable cells

Figure 1: Virtual skeleton computation process

its volume and maximum cross-section area of its members as “big enough” ensures convergence to the global optimum. In this case, modifying slightly the prescribed volume fraction will only change the final cross-sections of each bar without changing the ratio between them. Hence both the optimal truss and the scaled cross-section areas will stay the same and these are the objects that are used in this study.

2.1.2. Sensitivity analysis

The optimization problem (1) is solved using an Optimality Criteria approach (see for example [1, 33] and references therein) which requires first-order derivatives of the objective and constraint. For each bar, the sensitivity of the objective function is derived using the adjoint method and given by equation (2):

$$\frac{\partial f}{\partial \phi_i} = -\mathbf{u}_{1i}^T \frac{A_i E_i}{l_i} \mathbf{k}_i \mathbf{u}_{1i} \quad (2)$$

and the sensitivity of the constraint is given by equation (3):

$$\frac{\partial g}{\partial \phi_i} = A_i l_i \quad (3)$$

where \mathbf{u}_{1i} is the displacement vector at the nodes of the i -th bar.

2.1.3. Ground structure definition

As a base for the truss optimization, a layout of nodes between which bars are connected is created and constitutes the ground structure. For ease of use in this work, this layout is regular and has the shape of a rectangle in 2-D or a box in 3-D that correspond to the design domain of the continuum. This does not imply any loss of generality as recent works proposed a procedure to easily produce general ground structures for practically any geometric shape [34].

The optimal truss is a subset of this structure. As a matter of clearness, as the finite element mesh used in the second step is also called a ground structure [1], the latter will be referred to as the “grid” or “continuum grid” throughout the article.

In this method, a “cleaned” version of the ground structure has been used: a subset of it, containing only printable bars, whose angles with respect to the printing direction is less than the overhang angle. As all the chosen examples in this article are “long” because finding a printable optimal layout is then more challenging, the orientation of the part can thus be uniquely defined by its longest side. Furthermore, the printing direction is by default drawn vertically, as it is in reality, for convenience, see illustrations in Figure 2. Hence, the truss elements to be removed from the original ground structure depend upon the printing direction.

Figure 3 illustrates the allowable bar directions one can find in a ground structure (GS) of a half MBB beam, with respect to the printing direction. These structures appear tilted in order to match a vertical printing, as would be in reality.

2.2. Truss influence calculation

Once the truss is optimized based on the printable ground structure, a raster representation of it denoted by \mathbf{T} can be computed on a grid identical in size to that of the continuum. This raster representation is later used to

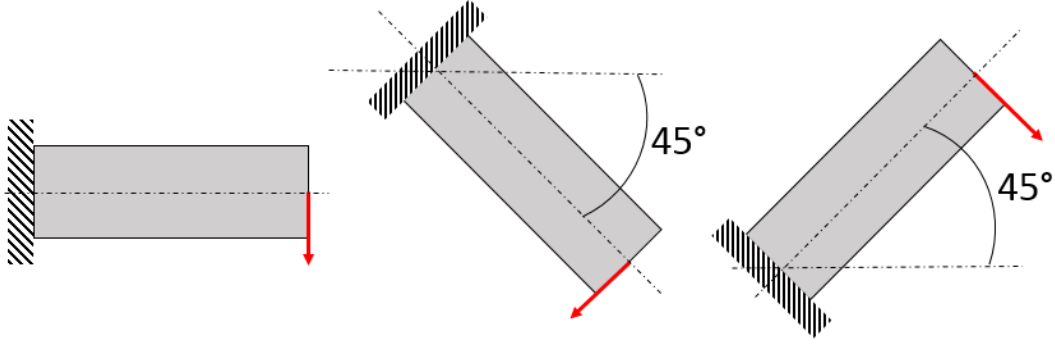


Figure 2: Definition of the printing direction demonstrated on a cantilever beam printed at 0° (left), at -45° (middle) and at $+45^\circ$ (right)

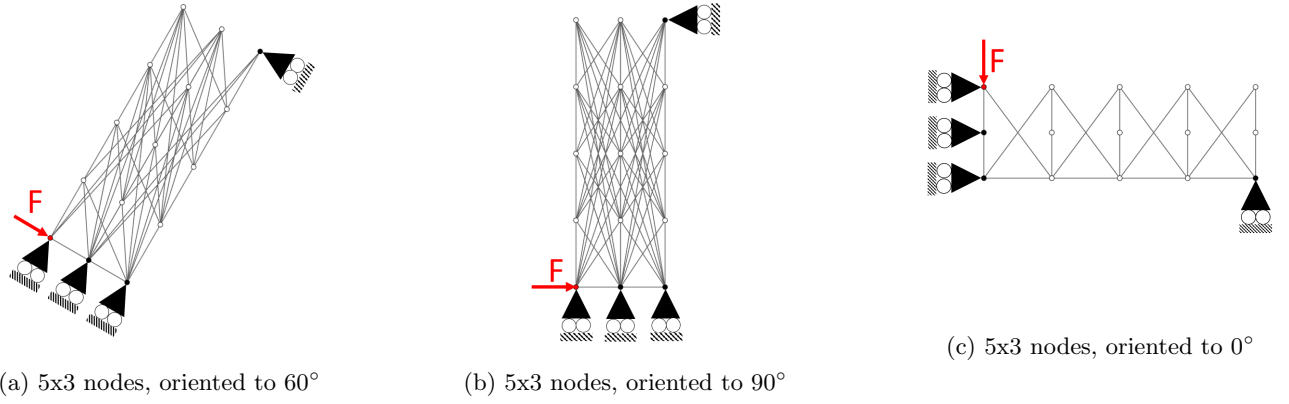


Figure 3: Examples of truss ground structures that vary according to the printing orientation.

influence the continuum-based optimization such that regions occupied by truss bars are prioritized. At this stage, this is important to note that the only role of this truss is to provide guides for material repartition in the continuum optimization. Its material has no essence nor impact on the continuum design compliance.

2.2.1. \mathbf{T} matrix mapping

A mapping is realized in order to build the matrix \mathbf{T} based on the optimal truss. This mapping only impacts the elements whose centers lay perpendicularly to the bar at a given distance from the bar. Let us consider a bar placed between the points A and B for example, as displayed in Figure 4. The maximum distance from the bar centerline until which a point is considered is d , i.e. only the points located in the blue zone are to be mapped. Points C and D will receive a finite value as a distance from the bar, while E will receive a very large value, ensuring the bar mapping will have no influence on the element density centered at E , as if the point was very far from the bar. To do so, the projection P of each point on the line is computed and the location of this projection – inside or outside the segment – is checked. It is enough here to evaluate the scalar product $\overrightarrow{PA} \cdot \overrightarrow{PB}$. If $\overrightarrow{PA} \cdot \overrightarrow{PB} > 0$ then P is outside the segment and the point shall be set aside. As D is farther than the expected distance from the bar centerline, meaning d , the element which is centered at D will not be mapped in \mathbf{T} and will not be influenced during the optimization. In 2-D,

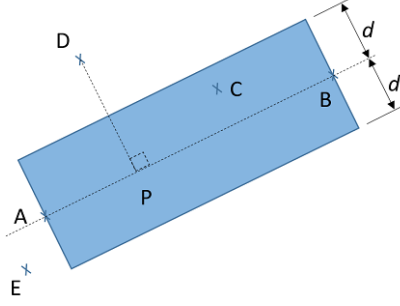


Figure 4: The region influenced by a truss bar AB .

the easiest approach to perform the calculations is to compute the line equations in the form $a \cdot x + b \cdot y + c = 0$. Then the distance d_C from a point $C(x_C, y_C)$ to the bar will be given by equation (4)

$$d_C = \frac{|a \cdot x_C + b \cdot y_C + c|}{\sqrt{a^2 + b^2}} \quad (4)$$

Once the influenced elements are found and their distances are computed, \mathbf{T} can be built in several different manners, as explained hereafter.

2.2.2. The different realizations of \mathbf{T}

Three ways of building \mathbf{T} are explored in the article, based on the same optimal truss presented in Figure 5. The first is the simplest: all the elements within a given distance d from the bars will appear as a pixel with the value $T=1$, as in Figure 6. This can be seen as a purely topological mapping, meaning that only the topology of the optimal truss determines the matrix \mathbf{T} . In the second approach, the optimized cross-section area of each bar will define the value assigned to each pixel by linear interpolation between 0 (non existing bar) and 1 (bar with the highest cross-section area). This approach is illustrated in Figure 7, and can be seen as a topology- and sizing-based mapping, as non-zero values of \mathbf{T} are assigned according to both the topology and the cross-section dimensions of the optimal truss. In the third way, the given distance mentioned in the first parametrization is replaced by a normalized version of the final cross-section areas: the larger the optimized cross-section, the larger it appears on \mathbf{T} , as illustrated in Figure 8. Then, all pixels within the specified distance receive the value $T=1$. The latter approach is again based on both topology and sizes of the truss, only that all non-zero values in \mathbf{T} are ones and the mapped distances are proportional to the cross-section sizes.

As the raster representation and the continuum grid have the same size, superimposing \mathbf{T} on the grid implies that each grid element only has one \mathbf{T} element over it. Then each grid element overlooked by an element which has a non-zero \mathbf{T} value will receive supplementary stiffness.

2.3. Continuum topology optimization

The second step of the methodology consists in the continuum optimization of the same problem as the discrete one. Yet, this phase is necessary for different reasons, mainly because concentrated stresses appear around the nodes where bars meet - refer to figure 1(d); the compliance of \mathbf{T} is high and a discrete optimization does not provide

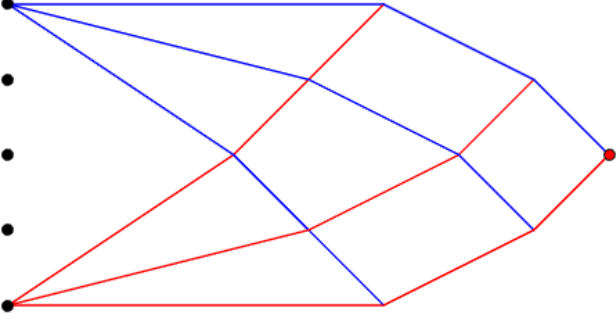


Figure 5: Optimized truss

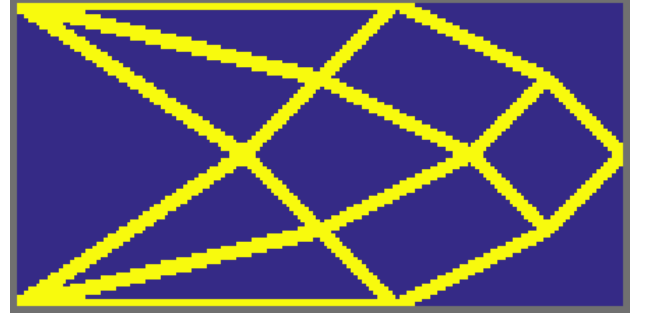


Figure 6: \mathbf{T} in configuration 1

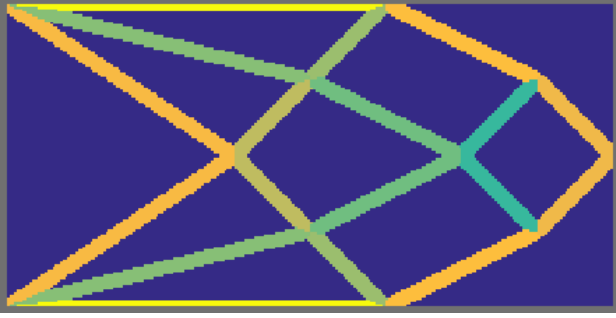


Figure 7: \mathbf{T} in configuration 2

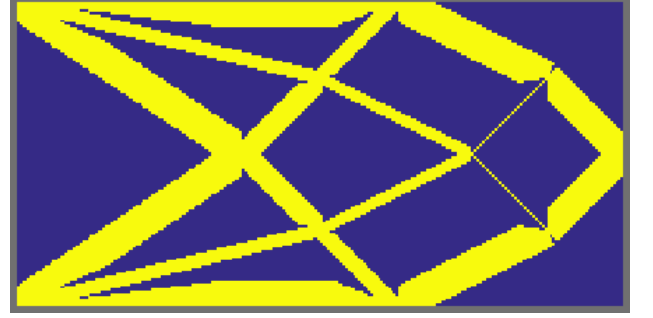


Figure 8: \mathbf{T} in configuration 3

the details (in terms of sizing, shape and even topology) that characterize a continuum one. This optimization is hereby performed on a continuum grid that is made of square finite elements for 2-D optimization and cubes for 3-D optimization. The target is to optimize their relative density, which defines how much they are filled with material. The aim of topology optimization is to find the best distribution of material in the design space, represented by a solid phase (density equal to one) and a void phase (density equal to zero). For this purpose, the mathematical element-based densities are transformed into physical ones using a density filter and a smooth Heaviside projection. The stiffness of each element depends on its physical density via a nonlinear interpolation function that effectively penalizes intermediate values between zero and one. The resulting problem formulation can be posed as follows

$$\left\{ \begin{array}{l} \min_{\boldsymbol{\rho}} f(\bar{\boldsymbol{\rho}}) = \mathbf{f}^T \mathbf{u}_2 \\ \text{s.t.} \left\{ \begin{array}{l} g(\bar{\boldsymbol{\rho}}) = \sum_{i=1}^{nelem} (\bar{\rho}_i v_i) - V^{**} \leq 0 \\ 0 \leq \rho_i \leq 1, \quad i = 1 \dots nelem \end{array} \right. \\ \text{with: } \sum_{i=1}^{nelem} (E_{\text{eff},i}(\bar{\rho}_i) \mathbf{k}_i^0) \mathbf{u}_2 = \mathbf{f} \end{array} \right. \quad (5)$$

where $\boldsymbol{\rho}$ is the vector of element-based design variables; $\bar{\boldsymbol{\rho}}$ is the vector of physical densities; \mathbf{f} is the external applied force; \mathbf{u}_2 is the field of nodal displacements; v_i is the element volume; V^{**} is the maximal admissible volume for the continuum structure; and \mathbf{k}_i^0 is the stiffness matrix of the i -th element for the case that $E = 1$.

The actual stiffness contributed by each element is determined by the effective Young's modulus of the element,

based on its physical density $\bar{\rho}_i$ and the optimal truss's influence T_i

$$E_{\text{eff},i} = E_{\text{SIMP}} (1 + T_i(\alpha - 1)) \quad (6)$$

with E_{SIMP} given by the Modified SIMP model [30, 35]

$$E_{\text{SIMP}} = E(\tilde{\boldsymbol{\rho}}) = E_{\min} + \tilde{\boldsymbol{\rho}}^p (E_0 - E_{\min}) \quad (7)$$

in which E stands for the interpolated Young's modulus; E_{\min} is a lower bound on the stiffness of void; E_0 is the stiffness of the base material; p is a penalty factor, typically chosen as equal to or larger than 3; and α is the influence factor, which physically defines how strong the influence is and how much the material repartition in the continuum design will stick to the truss. For avoiding numerical instabilities and for imposing length scale, a density filter [36, 37] that transforms the mathematical density distribution $\boldsymbol{\rho}$ to a physically viable distribution $\tilde{\boldsymbol{\rho}}$ is used

$$\tilde{\rho}_e = \frac{1}{\sum_{i \in N_e} H_{ei}} \sum_{i \in N_e} H_{ei} \rho_i \quad (8)$$

where N_e is the effective neighborhood of each material point (or finite element) e and H_{ei} is the filter weight factor. The layout defined by filtered densities tends to have gradual borders with intermediate densities. Therefore it is common to project these densities to 0-1 values using a smooth Heaviside projection [38]

$$\bar{\rho} = 1 - e^{-\beta \tilde{\rho}} + \tilde{\rho} e^{-\beta} \quad (9)$$

yielding the physical densities which are used both for finite element simulation and for manufacturing.

This optimization problem can be solved by first-order gradient-based algorithms. The Method of Moving Asymptotes – MMA by Svanberg [39] is used and the implementation in MATLAB is based on the 88-line topology optimization code [31] which was also used for generating the baseline results without the AM considerations. Solving by MMA requires the calculation of first-order derivatives which will be presented in the following.

The design variables are the densities ρ_i while both the objective function and the constraints are expressed with the physical densities. Hence, as detailed in [31], the sensitivity of a general functional ψ (which can represent either the objective or a constraint) is given by the chain rule:

$$\frac{\partial \psi}{\partial \rho_i} = \sum_{e \in N_i} \frac{\partial \psi}{\partial \bar{\rho}_e} \frac{\partial \bar{\rho}_e}{\partial \tilde{\rho}_e} \frac{\partial \tilde{\rho}_e}{\partial \rho_i} \quad (10)$$

where N_i is the neighborhood of the i -th element, and the derivatives $\frac{\partial \bar{\rho}_e}{\partial \tilde{\rho}_e}$ and $\frac{\partial \tilde{\rho}_e}{\partial \rho_i}$ can be derived from Eqs. (9) and (8), respectively.

The derivative of the objective function with respect to the physical densities is formulated using the adjoint method. The derivative with respect to a certain physical density $\bar{\rho}_e$, based on Equations (6) and (7) is given by

$$\frac{\partial f}{\partial \bar{\rho}_e} = -p \bar{\rho}_e^{p-1} (E_0 - E_{\min}) (1 + T_e(\alpha - 1)) \mathbf{u}_{2e}^T \mathbf{k}_e^0 \mathbf{u}_{2e} \quad (11)$$

where T_e is the value of the element e in the \mathbf{T} matrix, and \mathbf{u}_{2e} is the displacement vector of the element e . Finally, the derivative of the constraint can be expressed explicitly as

$$\frac{\partial g}{\partial \bar{\rho}_e} = v_e. \quad (12)$$

2.4. Evaluation criteria

185

In this study, the final design of the part is of interest. We thus consider that even if external supports need to be created due to the tilted printing direction, they can be easily suppressed by machining. The eventual external supports created are thus considered easily removable by machining. The amount of lost material in building these external supports is not taken into account. Conversely, internal supports are usually not likely to be machined, especially for 3-D parts, where the sections to be removed may not be accessible by the cutting tool.

Hence, the two criteria used for evaluating the design are the *structural performance* (measured by the compliance $\mathbf{f}^T \mathbf{u}_2$) and the *printability*. The compliance c_m is directly computed by a finite element analysis of the continuum and compared to the compliance c_b of the reference baseline solution. In the case of an influenced continuum design, this criterium needs to be recomputed not to take the virtual truss stiffness into account. The performance drop measure PD is then given by

$$\text{PD} = \frac{|c_m - c_b|}{c_b} \cdot 100. \quad (13)$$

In other words, PD is the percentage of increase in compliance compared to the reference design which is expected to be the stiffest, i.e. will have the lowest compliance. The printability is evaluated in a manner inspired by Driessen [40]: the edge of the continuum structure is multiplied by dot product with the printing direction \mathbf{n} . This edge is defined by its normal, the density gradient $\nabla \bar{\rho}$. The dot product is given by Equation (14), θ being the angle formed by the two vectors

$$\mathbf{n} \cdot \nabla \bar{\rho} = \|\mathbf{n}\| \cdot \|\nabla \bar{\rho}\| \cos \theta \quad (14)$$

Edge detection can be realized by using the Sobel, Prewitt or Roberts operator [41] convoluted with the density matrix. For convenience and symmetry, the Prewitt operator, which kernels are given by Equation (15), is used:

$$\mathbf{K}_x = \begin{bmatrix} -1 & 0 & 1 \\ -1 & 0 & 1 \\ -1 & 0 & 1 \end{bmatrix}, \quad \mathbf{K}_y = \begin{bmatrix} 1 & 1 & 1 \\ 0 & 0 & 0 \\ -1 & -1 & -1 \end{bmatrix} \quad (15)$$

In the actual implementation, the native MATLAB function `imgradientxy` [42] that computes the gradients both in the x and y directions is used. This function can be associated with the Prewitt kernels and its main advantage compared to convolution is that values outside the working area boundaries are assumed to equal the border values. The dot product (14) can be normalized, which allows to detect easily all the unprintable pixels. Then, these pixels are counted and their number is divided by the total available amount of material, giving the relative measure of unprintability

$$\text{UP} = \frac{\text{number of unprintable pixels}}{\text{quantity of available material}}. \quad (16)$$

190

Clearly, because the gradient of the image is a numerical derivation taking into account the neighboring cells (or pixels), even small unprintable patterns will involve several pixels. Hence, it is expected that the unfeasible portion reported will be greater than the one in reality. Using a Roberts operator would reduce the issue as it uses a kernel of 2×2 instead of 3×3 for Sobel and Prewitt, but it is not symmetric. Accordingly, overhang patterns are, in fact, printable in a small distance [17]. This means that little points appearing in the dot product are likely to be

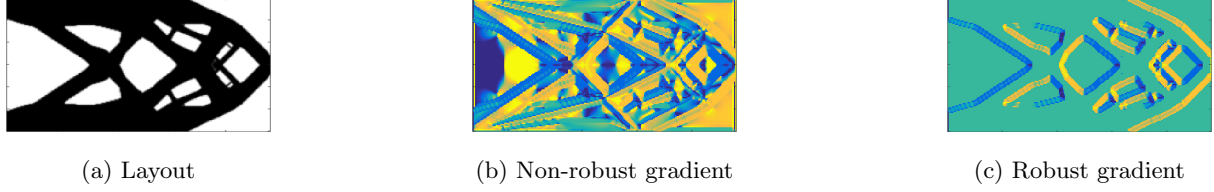


Figure 9: Illustration of the robust gradient computation.

manufacturable. The direct consequence is that the number presented as unprintable proportion is the *maximal* unprintable proportion. Despite these limitations, it appears that this criterion is the best available.

It is also worth noting that due to numerical precision, it is necessary either to work with crispy designs – basically only 0 and 1, or to make the calculations robust to intermediate densities. The problem comes from the presence of the gradient norm in the denominator for the normalization. If the designs are not crispy, there is a very small gradient appearing for several finite elements, with order of magnitude of 10^{-16} . Once normalized, these small gradients will appear in the denominator, making the dot product result irrelevant. One way of improving robustness of the tool is to limit the elements gradient norms within three orders of magnitude. Figure 9 shows the robust versus non-robust gradient analysis.

3. Numerical examples in 2-D

The proposed approach is intended for reducing the amount of support material required for additive manufacturing of complex 3-D designs obtained by topology optimization. Therefore it should be examined on 3-D cases in order to evaluate its performance and compare it fairly to other approaches suggested recently. Nevertheless, in order to illustrate the effect and gain of the proposed method, this latter is first applied to a set of examples in 2-D. Several results are presented and investigated in this section, while the influence of the chosen parameters is discussed later on in Section 4.

3.1. Cantilever beam

The 2-D cantilever to optimize is represented in Figure 10. The gray region is the continuum ground structure: a $n_{\text{cant},x} \times n_{\text{cant},y}$ rectangle, subjected to a point force \vec{F} .

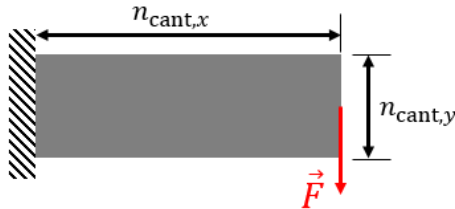


Figure 10: Setup of the cantilever problem.

The cantilever examples are run on a grid of 200×100 Q4 elements with a filter radius of 2 and a penalization $p = 3$. Regarding the virtual skeleton method, the truss is created from a 9×5 nodes ground structure, and the



Figure 11: Optimal cantilever trusses for different printing directions

multiplying parameter is $\alpha = 5$. The number of design iterations is limited to 2000 for the truss and 200 for the continuum. In our implementation of the Heaviside projection, β begins at 1 and doubles after each 50 iterations or if the design change is small enough (0.01).

One very important feature of this method is its ability to cope with low volume fractions, meaning the available amount of material within the total volume of the design domain. While other methods, filter-based for example, presumably need more material to assure a necessary level of support, this one can deal with a lower amount of material. One simply has to ensure that the distance parameter in \mathbf{T} , which is expressed as a number of pixels or elements, is small enough in order to satisfy the volume constraint.

Table 1 presents the results obtained for a volume fraction of 60% while Table 2 presents the results for a volume fraction of 30%. In this latter case, the distance has been reduced from 3 to 1.5. In the tables, the ‘Results’ column presents the obtained compliance (c), the performance drop (PD) if relevant and finally the unprintability (UP) in percentage. The ‘Printability plot’ column displays the unprintable pixels for the optimized layout, while the ‘Ref. print. plot’ column illustrates the unprintable pixels for the baseline design with the specified printing direction. For clarity, the layouts and the unprintable patterns are displayed in a vertical printing direction, as in reality. The raster representation of the optimal trusses obtained are presented in Figure 11.

Obviously, a trade-off must be found between structural performance and printability. This is especially clear when examining the result in Table 2 with a printing orientation of -60° . The gradient gives only unprintable points, meaning that the part is essentially 100% printable. At the same time, the performance drop in this case is 36.61%, making the part less efficient.

3.2. MBB beam

The MBB beam is a classical example taken in topology optimization. The continuum ground structure is loaded by a force \vec{F} in its middle, while supported by two hinges at its extremities. The problem to solve is illustrated in Figure 12, both with the full beam considered and with the half beam that uses symmetry as to alleviate the computational burden. Although these two models possess the same analytical solution, the composition of the discrete ground structure in the proposed approach is different in each case. Thus, one can expect different outputs.

It should be noted that if the beam is designed *and manufactured* as two symmetric halves, then the two halves must be welded later on. To the authors’ knowledge, welding of 3-D printed parts has not yet been studied thoroughly

Table 1: Cantilever optimization with a volume fraction of 60%



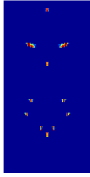
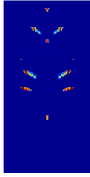

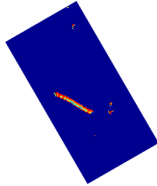
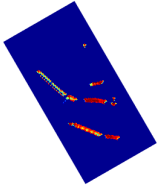
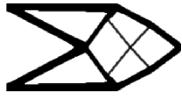

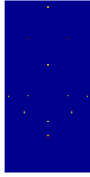
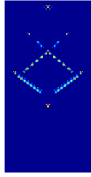

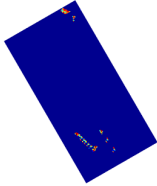
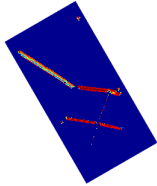
Case	Results	Layout	Printability plot	Ref. print. plot
Baseline	$c = 54.16$ UP = 3.68% for 90° UP = 6.38% for -60°		N/A	N/A
Print at 90°	$c = 55.15$ PD = 1.83% UP = 2.28%			
Print at -60°	$c = 58.58$ PD = 8.16% UP = 2.63%			

Table 2: Cantilever optimization with a volume fraction of 30%

Case	Results	Layout	Printability plot	Ref. print. plot
Baseline	$c = 103.19$ UP = 10.47% for 90° UP = 15.17% for -60°		N/A	N/A
Print at 90°	$c = 96.1$ PD = -6.87% UP = 0.43%			
Print at -60°	$c = 140.97$ PD = 36.61% UP = 3.13%			

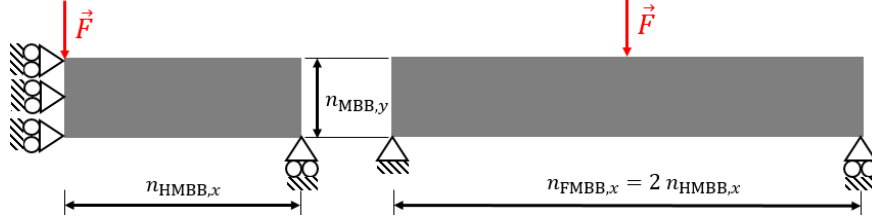


Figure 12: Half MBB beam (left) VS full MBB beam (right)

and may introduce difficulties when aiming to manufacture parts that are bigger than the machine’s capabilities. This point is out of the scope of the current study, meaning that the beam is assumed to be manufactured in two parts and welded later without any change in performance.

The numerical experiments are realized on a “long” beam. The total length of the full beam is 480x80 elements (240x80 elements for the symmetrical model). The filter radius is 1.5, the penalization factor is 3, the volume fraction is 60% and the distance is 2. The results are reported in Table 3 for the full beam and in Table 4 for the half beam, for various printing directions. Furthermore, the \mathbf{T} matrix is displayed below or next to the continuum optimal design. For clarity of the presentation, the layouts and printability plots of the full beam are presented in the natural (horizontal) direction of 0° in all cases.

It can be noticed from Table 2, in the case where the part is printed at 90° , that the proposed method can produce better outputs than the reference. Although this improvement is not systematic, several elements increase the probability of its occurrence: the initial design design is close to being fully printable, leaving small room for important design changes and the volume fraction is low enough to ensure that all the material sticks to the truss location. The computed truss is a global optimum to the problem and is fully printable, giving advantage to this case over the standard optimization. However, due to its size, the continuum problem converges almost exclusively toward local optima. Hence, the choice of parameters is crucial to realize a better optimization. The next section is dedicated to the parametric study.

4. Parametric study

Many different parameters are involved in the proposed method and impact it in a fashion which is sometimes counter-intuitive. The influence of the main parameters is investigated here in order to shed light on the preferable choice of their values. In the test cases herein, if not stated otherwise, the SIMP penalization is 3, the distance is 3, the filter radius is 1.5, the volume fraction is 60%, \mathbf{T} is in the second configuration and α is 5.

4.1. Maximum overhang angle

The maximum overhang angle depends on the technology and the machine used. To that extent, it is an external parameter that cannot be optimized in the simulation. It is an input. Nevertheless, it is interesting to show the effectiveness of the method for different possible angles. Figure 13 presents respectively the ground structure, optimal truss, \mathbf{T} and optimal continuum designs for maximum overhang angles of 30° , 45° and 60° of a cantilever of geometric

Table 3: Full MBB beam results




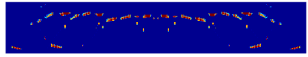
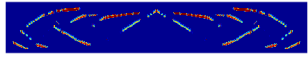


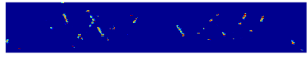
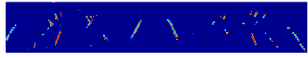



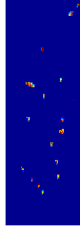
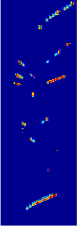

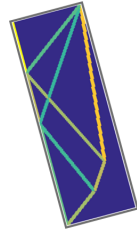
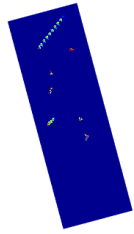
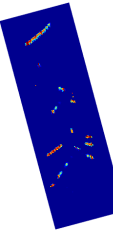
Case	Results	Layout	Printability plot	
			Ref.	print. plot
Baseline	$c = 83.25$ UP = 14.74% for 0° UP = 6.48% for 90°		N/A	
Print at 0°	$c = 89.94$ PD = 8.04% UP = 7.72%	 	 	
Print at 90°	$c = 84.34$ PD = 1.31% UP = 3.84%	 	 	

Table 4: Half MBB beam results

Case	Results	Layout		Printability plot	Ref. print. p
Baseline	$c = 166.49$ UP = 6.09% for 90° UP = 4.74% for -75°			N/A	N/A
Print at 90°	$c = 169.63$ PD = 0.32% UP = 2.5%				
Print at -75°	$c = 170.17$ PD = 2.21% UP = 2.26%				

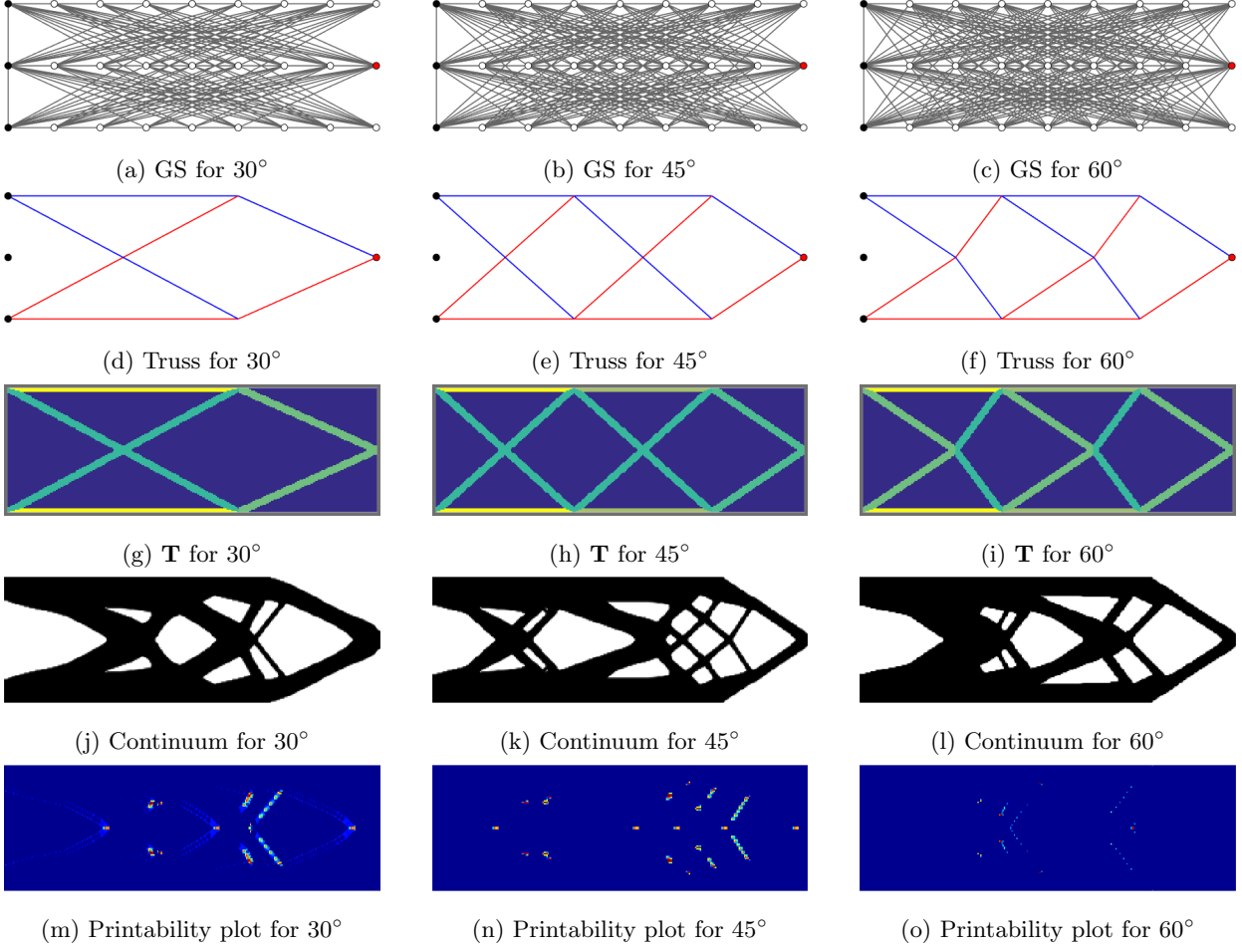


Figure 13: Main step results for a maximum overhang angle of 30° (left), 45° (middle) and 60° (right) with a printing direction of 90°

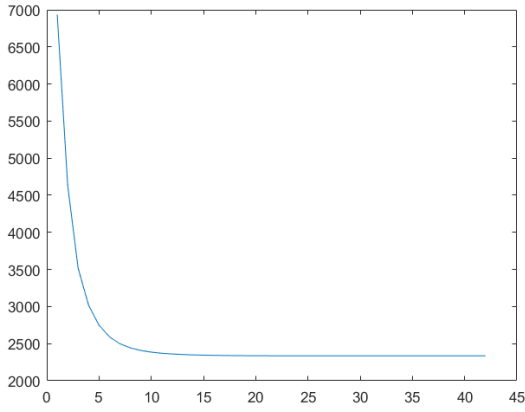
ratio 3:1. It should be noted that if a truss ground structure is not fine enough, it is possible that no optimal truss could be found.

From a convergence point of view, both the truss and the continuum are monotonous, as can be seen from Figure 14. These are the convergence histories of the truss and the continuum of the case of an overhang angle of 30° .

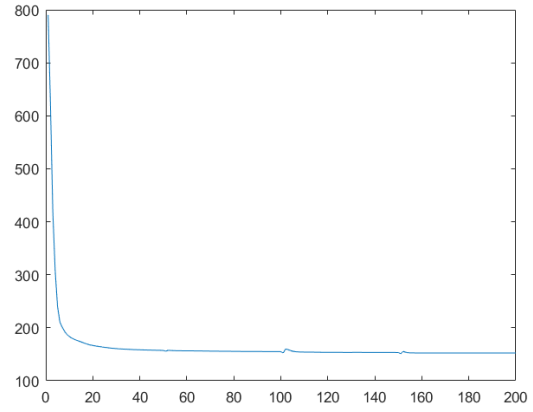
4.2. Printing orientation

One of the first decisions to be made regards the optimal orientation angle for the truss, which is called here ‘printing direction’. This is in fact a crucial optimization problem in its own right – if a certain part is to be printed without re-designing it by topology optimization, then naturally one would like to find the best position of the part in the cubicle such that support material is minimized. In the virtual skeleton approach, this aspect can be partly considered when determining the orientation of the truss.

Figure 15 presents the compliance values of the optimized truss structures, found for a range of printing angles. These results were obtained by varying the printing angle by increments of fifteen degrees, and running the truss



(a) Convergence of the truss



(b) Convergence of the continuum

Figure 14: Convergence history plots for a 30° overhang angle

optimization phase within the limit of 2000 optimization iterations for each run. In the graphs, the largest compliance values were artificially cut at the values of 2000, 600 and 3000 for the cantilever, the half and the full MBB beam respectively. This was in order to ease the reading of the graphs, as only the minimal values are of interest.

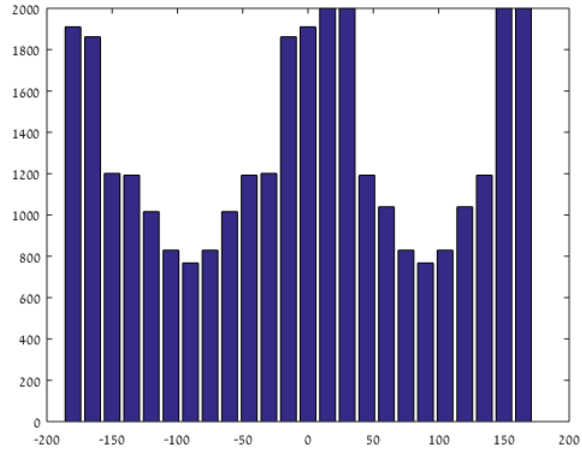
First, it is important to note here that there is no necessary continuity in these graphs. Even though some regular patterns seem to appear, it is possible that for some printing angles, there cannot be found any structure able to hold the load, unless when working with a heavily meshed ground structure.

As for the results themselves, it is noticeable that several orientations can give closely optimal trusses. For the half-MBB beam, the equally best orientations are $+/-90^\circ$ and 180° (upside down printing), while it is $+/-90^\circ$ only for the full-MBB beam. It is also clear that the best printing directions are $+/-90^\circ$ for the cantilever. Nevertheless, the continuum optimization is by nature not limited to specific directions as it fills material more freely. Then, in some cases, the indication given by the graph does not match the final continuum result, as shown in Table 5. In the table, the compliance of the optimized continuum half-MBB beam is presented, achieved with various printing orientations. In these cases, the discrete ground structure was meshed by 9×5 nodes and the continuum mesh possessed 180×60 elements.

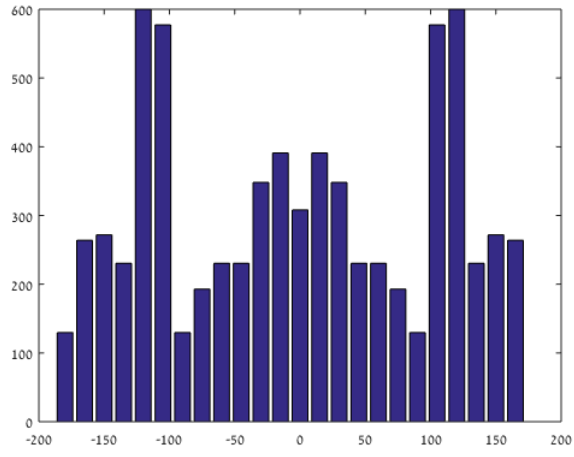
Table 5: Compliance of a continuum half-MBB beam

<i>Orientation</i>	-90°	-75°	-60°	-45°
<i>Truss compliance</i>	805	843.12	945.68	970.24
<i>Continuum compliance with truss influence</i>	174.37	171.12	173.44	176.2

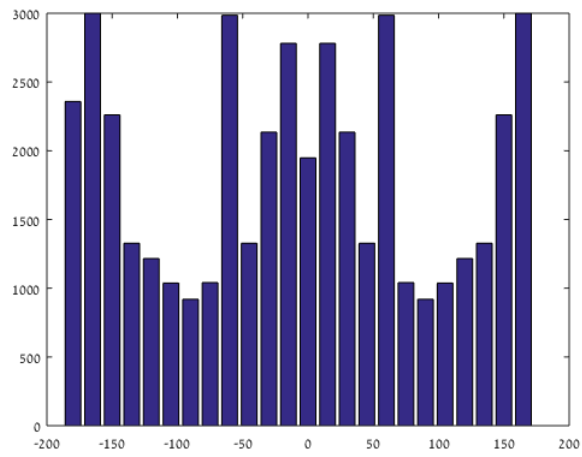
If the continuum optimization followed directly the indication given by the optimal truss, the structure obtained for an orientation of -90° should have been better than the one obtained for an orientation of -75° . Nevertheless,



(a) compliance by printing direction for the cantilever



(b) compliance by printing direction for the half-MBB beam



(c) compliance by printing direction for the full-MBB beam

Figure 15: Graphs of truss compliances with respect to the printing angle

it can be seen that the orientation of -75° is the best choice for the continuum. This demonstrates that choosing the optimal truss orientation does not guarantee the best results for the continuum optimization, and in practice several orientation angles should be examined. Still, from the author's own experience, the optimal truss angle gives a reasonable interval of the ultimate optimal printing direction.

4.3. Distance parameter in \mathbf{T}

The mentioned distance parameter d has a direct influence on the final design, as the larger d is, the more elements are influenced and thus prioritized. This can be observed in Figures 16 to 18 that present the \mathbf{T} matrix image for the cantilever example, for several distance values. For a given volume fraction, a smaller d leaves more

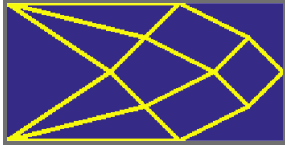


Figure 16: \mathbf{T} for $\text{dist}=2$



Figure 17: \mathbf{T} for $\text{dist}=5$



Figure 18: \mathbf{T} for $\text{dist}=8$

design freedom in the continuum phase as less material is pushed towards the virtual skeleton. Consequently, smaller d values are expected to lead to continuum designs that have better performance in terms of compliance but also have more unprintable regions. This effect is shown in Table 6, which presents compliance and unprintability results for a cantilever printed at 90° for different values of d . There is an obvious trend of increase in compliance with and increase in d , while a reduction in unprintability is also observed but is not as monotonous.

Table 6: Compliance and printability for different values of d

	$d = 1$	$d = 2$	$d = 3$	$d = 4$	$d = 5$
<i>Compliance</i>	179.04	182.81	188.33	193.83	202.59
<i>Unprintability</i>	3.25%	1.38%	1.10%	1.44%	1.23%

4.4. Number of truss nodes

Two main hypothesis can be made, relatively to the coarseness of the ground structure. First, it can be assumed that an optimization based on densely populated ground structure will produce designs with better compliance, as the optimization algorithm can pick a better solution for the truss, hence a better one for the continuum. Secondly, one could assume that more nodes should induce a better printability. Experience shows that such trends do not exist, which is rather counter-intuitive. Table 7 presents compliance of optimal truss, continuum and unprintability (UP) for different truss ground structure resolutions in the case of a cantilever printed at 90° with a 50% volume fraction. The two table entries are the number of nodes along the X axis – columns – and the number of nodes along

Table 7: Influence of the coarseness of the discrete ground structure

	7 nodes	9 nodes	11 nodes	13 nodes
3 nodes	$c_{\text{truss}} = 2,103$	$c_{\text{truss}} = 2,129$	$c_{\text{truss}} = 2091$	$c_{\text{truss}} = 2,066$
	$c_{\text{cont}} = 223.93$	$c_{\text{cont}} = 179.93$	$c_{\text{cont}} = 180.84$	$c_{\text{cont}} = 274.63$
	UP = 0.72%	UP = 2.35%	UP = 1.01%	UP = 0.65%
5 nodes	$c_{\text{truss}} = 1,998$	$c_{\text{truss}} = 1,995$	$c_{\text{truss}} = 2,004$	$c_{\text{truss}} = 1,967$
	$c_{\text{cont}} = 196.60$	$c_{\text{cont}} = 197.07$	$c_{\text{cont}} = 202.82$	$c_{\text{cont}} = 239.42$
	UP = 2.47%	UP = 2.57%	UP = 3.22%	UP = 0.60%
7 nodes	$c_{\text{truss}} = 1,964$	$c_{\text{truss}} = 1990$	$c_{\text{truss}} = 1,995$	$c_{\text{truss}} = 1,948$
	$c_{\text{cont}} = 219.78$	$c_{\text{cont}} = 236.13$	$c_{\text{cont}} = 220.76$	$c_{\text{cont}} = 205.98$
	UP = 0.99%	UP = 1.56%	UP = 0.69%	UP = 0.68%



(a) 9x3 truss



(b) 9x3 continuum



(c) 9x7 truss



(d) 9x7 continuum

Figure 19: Comparison of the results from two different ground structures

the Y axis – rows, where the axis system is defined in Figure 10. The aspect ratio of the cantilever is 3:1 (300x100 elements), as pictured in Figure 19.

Regarding the first assumption, it is clear from the table that a fine ground structure does not necessarily produces better outputs. This is even true for the truss, as the optimum found each time is a local minimum due to the large number of variables. The cases 9x3 ($c = 179.93$) versus 9x7 ($c = 236.13$) nodes are taken as continuum examples. The limited amount of available material aggregates within the given distance of the optimal truss, constraining the design, as pictured in Figure 19. This explains that the compliance of the continuum may be better for coarser ground structures. This reason should give credit to the second hypothesis, assuming that a finer ground structure produces more printable designs.

As can be seen from Table 7, although there seems to be a trend of better printability for finer meshes, there is no monotonous pattern. Indeed, the continuum design based on 9x5 nodes is more printable (UP= 2.57%) than the one based on 11x5 nodes (UP= 3.22%).

4.5. \mathbf{T} matrix configurations

The different \mathbf{T} matrix configurations proposed impact differently the design, as they influence the continuum optimization in different fashions. As the distance parameter is fixed in the first configuration, \mathbf{T} transmits to the algorithm the bar locations, while the second configuration is a weighted version of it. Thus, the design is less constrained and better results are expected. As the third configuration is also weighted, but in the way that more important bars will influence more grid elements, it is expected that its use should be limited to designs with a large volume fraction.

Tests were performed on the best case of Table 7, with different \mathbf{T} matrix configurations and presented in Table 8. In this case, and from the authors' experience, in most cases, the second configuration gives the best results.

Table 8: Compliance and printability for different configurations of \mathbf{T}

	configuration 1	configuration 2	configuration 3
<i>Compliance</i>	180.71	179.93	202.34
<i>Unprintability</i>	1.91%	2.35%	4.77%

4.6. Multiplicative parameter α

The same analysis can be performed with the multiplicative parameter α : constraining a structure to adapt to the virtual skeleton – by increasing the value of α – tends in general to improve its printability to the detriment of compliance. Figure 20 shows the compliance and the unprintability UP as a function of α . While the compliance tends to deteriorate with an increasing α , the printability tends to improve.

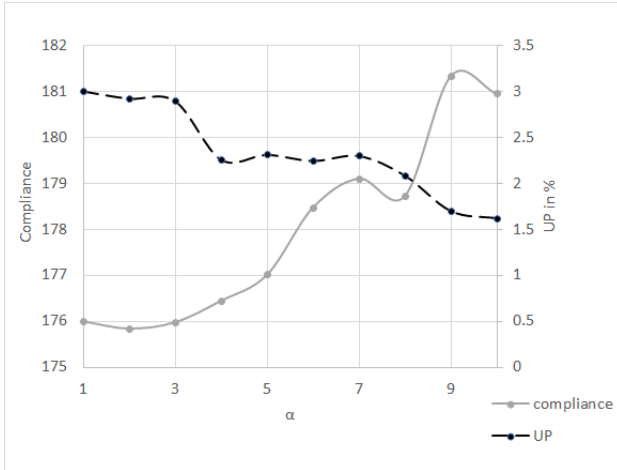


Figure 20: Compliance and unprintability as a function of α

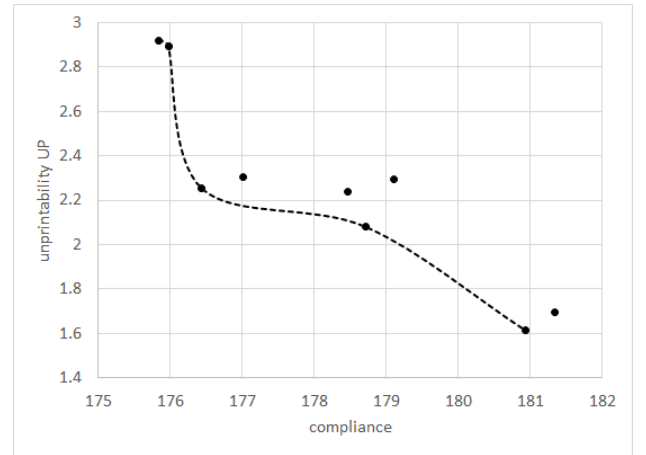


Figure 21: Trade-off chart of compliance versus printability

4.7. A remark regarding the role of the final user

It has been shown in the previous sections that different parameters influenced both compliance and printability. It has also been explained that the differences in the technologies allowed to print an angle more or less restricted than the 45° that has been employed in the simulations. If the set of results of the previous section is depicted as a trade-off chart, as in Figure 21, a Pareto front – in dashed line – clearly appears. A similar Pareto frontier would have appeared if the chart was linked to the other parameters studied. That means that as there is no global optimum for the choice of parameters, the user needs to choose the appropriate weighting pattern according to his/her own constraints and the technology that is used.

5. Numerical examples in 3-D

Relying on the two-dimensional demonstrative cases and on the subsequent parameter investigation, the extension to three-dimensional topology optimization accounting for overhang limitations using a virtual skeleton is hereby presented. In this section, some details regarding the generation of \mathbf{T} based on the distance between truss bars and grid elements are presented. This is followed by a few examples involving 3-D design scenarios.

5.1. Computing the distance between bars and grid elements

Lines are hyperplanes in dimension 2, but not in dimension 3. This means that in order to define a bar or a line in the same fashion that it was defined in 2-D, one would need two equations, representing two intersecting planes. Using this approach to build the distance matrix is not efficient.

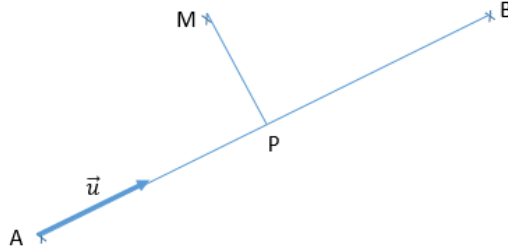


Figure 22: Projection computation problem

In order to find the projection P of the point M onto the segment AB, as sketched in Figure 22, one has to calculate the coordinates of P such that the scalar product $\overrightarrow{AP} \cdot \overrightarrow{PM} = 0$. With \vec{u} the direction vector of AB, the distance d_M between M and the line AB is given in vector notation by:

$$d_M = \frac{\|\overrightarrow{AM} \times \vec{u}\|}{\|\vec{u}\|} \quad (17)$$

$\overrightarrow{AM} \times \vec{u}$ being the cross product of the vectors \overrightarrow{AM} and \vec{u} and $\|\vec{u}\|$ is the norm of the vector \vec{u} .

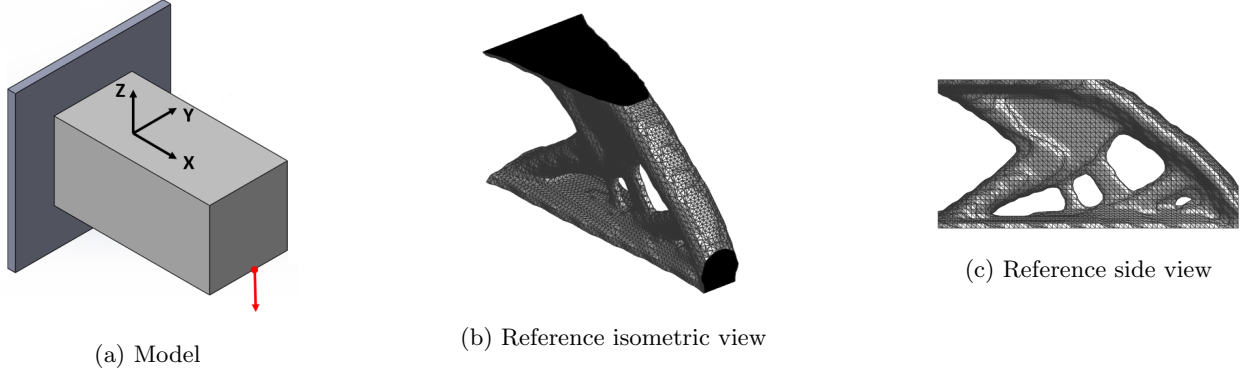


Figure 23: Optimized layout of a 3-D cantilever without considering the printing direction

The actual coordinates of P can be found by minimizing this distance:

$$\begin{cases} x_P = k \cdot u_x + x_A \\ y_P = k \cdot u_y + y_A \\ z_P = k \cdot u_z + z_A \end{cases} \quad \text{with} \quad k = \frac{u_x(x_M - x_A) + u_y(y_M - y_A) + u_z(z_M - z_A)}{u_x^2 + u_y^2 + u_z^2} \quad (18)$$

Then while printing along the X-axis for example, the points whose projection does not belong to the segment AB can be segregated by comparing the x -coordinates.

5.2. 3-D topological designs

One of the evident advantages of the virtual skeleton method is its direct extension to implementation in three dimensions. This generalization needs to take into account the dimension change, as the printing orientation for example is now a solid angle and must be defined by two parameters.

As for the 2-D case, our formulation is based on the classical density-based approach to topology optimization. For efficient treatment of the structural analysis equations, a multigrid preconditioned conjugate gradient (MGCG) solver is employed and the implementation for topology optimization presented by Amir et al. [43] is followed. As a demonstrative example, the optimization of a cantilever structure subjected to a point load at the bottom of its free edge is examined. The continuum problem is modeled using a structured grid consisting of $64 \times 32 \times 32$ cubes; the allowable volume fraction is 0.15; the modified SIMP penalty is $p = 3.0$; and the density filter radius is $\sqrt{3}$. The reference layout, obtained without considering the printing direction, is presented in Figure 23.

The cantilever is optimized for two printing directions. For the case of printing in the X-direction, the truss ground structure, the optimized truss and the resulting influenced continuum layout are displayed in figure 24. Truss optimization is realized by Linear Programming. Results of printing in the Z-direction are presented in figure 25. The compliance obtained are $c = 10.68$ for the standard optimization, $c = 11.56$ for the influenced solution printed along the X-axis and $c = 12$ along the Z-axis. This gives a 8.24% performance drop in the first case and 12.36% in the second one.

Regarding the printability, an improvement is observed. The standard optimization offers an unprintability of 4.99% when printed along the X-direction and 21.23% when printed along the Z-direction. The influenced design presents respectively $UP=2.28\%$ in X and 14.63% in Z.

An improvement is also noted regarding the computational burden, as the continuum optimization with standard procedures takes almost five times the time needed to reach convergence for the influenced designs under the same parameters. This is partly explained by the fact that in the influenced case, the algorithm stopped because the difference between the designs in two consecutive iteration was below the defined threshold. In the standard case, the algorithm stopped because it reached the maximum number of allowed iterations. Furthermore, the computation time for the rest of the procedure is negligible. Less than 3.5 seconds are needed to draw the ground structure and solve the truss while almost 1 hours and 20 minutes are needed to solve the continuum problems based on this truss.

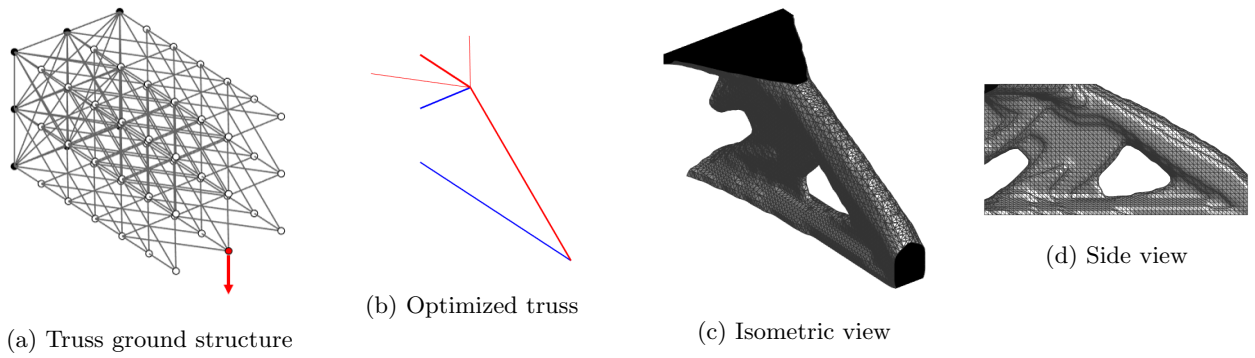


Figure 24: Topology optimization of a 3-D cantilever with a virtual skeleton for printing in the X-direction.

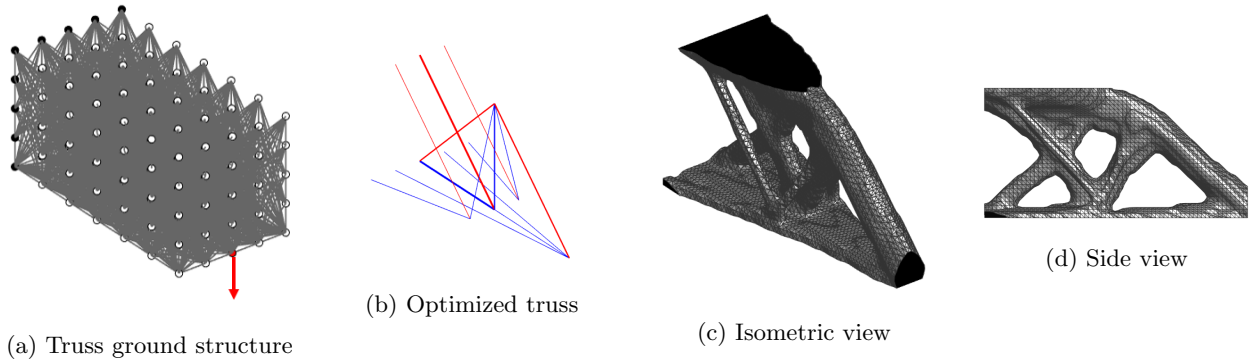


Figure 25: Topology optimization of a 3-D cantilever with a virtual skeleton for printing in the Z-direction.

6. Discussion

The present article proposes a new method for designing additive manufactured optimized components, based on well-established topology optimization procedures. If theoretically, the method can also be used for designs under other physics, such as 3D heat conduction, only results for structural mechanics were presented. The suggested

400 approach accounts for the maximum achievable overhang, which is a central limitation of 3-D printing. It consists of solving sequentially two structural optimization problems – the first on a discrete truss-based model and the second on a continuum-based model. The allowable overhang is considered in the truss optimization, and the resulting optimal truss is projected on to the continuum so that it influences the material distribution in the continuum optimization. Numerical results show that the designs obtained by this approach exhibit improved printability as
405 they have fewer overhanging features – in some cases practically no supporting material will be required for printing the optimized design.

There are several advantages to this method, compared to other approaches proposed in the literature. 1) The method relies on two well-known and highly efficient procedures for truss-based and continuum-based optimization; 2) Compared to standard topology optimization, there is no supplementary computational burden: the continuum
410 is computed exactly in the same manner and the initial generation of the virtual truss skeleton is extremely cheap in computational terms; 3) Adding a first step of optimizing a truss structure also gives a first optimal “guess” which allows to reduce the number of further iterations in the continuum phase; 4) Changing the desired printing direction only means modifying the truss ground structure, and virtually any angle can be examined; and 5) The generalization to design domains of general shape and models using unstructured grids is straightforward.

415 Based on the truss optimization, it was shown that the virtual skeleton approach allows to define the magnitude of the optimal printing direction and can provide layouts that have good printability with a limited performance drop. The different parameters studied also showed that a trade-off should be found between constraining the continuum optimization so that better printability is achieved, and relaxing it so that the ultimate performance is not severely compromised. An important conclusion regarding the initial truss ground structure is that it must be relatively
420 coarse in order to guide the continuum optimization without over constraining it.

Future research will focus on developing a 3-D ground structure that accounts for two input angles, allowing it to rotate in the whole solid angle. Accordingly, the tool for evaluating unprintable zones in 3-D will be developed and implemented as to measure the component printability. Finally, the implementation will be extended to accommodate large-scale topology optimization on highly refined finite element models.

- 425 [1] M. P. Bendsøe, O. Sigmund, Topology optimization: theory, methods and applications, Springer, Berlin, 2003.
- [2] O. Sigmund, K. Maute, Topology optimization approaches, *Structural and Multidisciplinary Optimization* 48 (6) (2013) 1031–1055.
- [3] J. Deaton, R. Grandhi, A survey of structural and multidisciplinary continuum topology optimization: post 2000, *Structural and Multidisciplinary Optimization* 49 (1) (2014) 1–38. doi:10.1007/s00158-013-0956-z.
430 URL <http://dx.doi.org/10.1007/s00158-013-0956-z>
- [4] M. Bruggi, C. Cinquini, Topology optimization for thermal insulation: an application to building engineering, *Engineering Optimization* 43 (11) (2011) 1223–1242.
- [5] T. E. Bruns, Topology optimization of convection-dominated, steady-state heat transfer problems, *International Journal of Heat and Mass Transfer* 50 (15) (2007) 2859–2873.
- 435 [6] J. Alexandersen, N. Aage, C. S. Andreasen, O. Sigmund, Topology optimisation for natural convection problems, *International Journal for Numerical Methods in Fluids* 76 (10) (2014) 699–721.
- [7] S. Bose, S. Vahabzadeh, A. Bandyopadhyay, Bone tissue engineering using 3d printing, *Materials Today* 16 (12) (2013) 496–504.
- [8] K.-T. Zuo, L.-P. Chen, Y.-Q. Zhang, J. Yang, Manufacturing-and machining-based topology optimization, *The International Journal of Advanced Manufacturing Technology* 27 (5-6) (2006) 531–536.
440
- [9] J. K. Guest, M. Zhu, Casting and milling restrictions in topology optimization via projection-based algorithms, in: *ASME 2012 International Design Engineering Technical Conferences and Computers and Information in Engineering Conference*, American Society of Mechanical Engineers, 2012, pp. 913–920.
- [10] C. W. Hull, Apparatus for production of three-dimensional objects by stereolithography, uS Patent 4,575,330 (Mar. 11 1986).
445
- [11] H. Lipson, M. Kurman, *Fabricated: The new world of 3D printing*, John Wiley & Sons, 2013.
- [12] D. Gu, W. Meiners, K. Wissenbach, R. Poprawe, Laser additive manufacturing of metallic components: materials, processes and mechanisms, *International materials reviews* 57 (3) (2012) 133–164.
- [13] W. E. Frazier, Metal additive manufacturing: a review, *Journal of Materials Engineering and Performance* 23 (6) (2014) 1917–1928.
450
- [14] T. T. Le, S. A. Austin, S. Lim, R. A. Buswell, R. Law, A. G. Gibb, T. Thorpe, Hardened properties of high-performance printing concrete, *Cement and Concrete Research* 42 (3) (2012) 558–566.
- [15] K. V. Wong, A. Hernandez, A review of additive manufacturing, *ISRN Mechanical Engineering* 2012.
- [16] I. Gibson, D. W. Rosen, B. Stucker, et al., *Additive manufacturing technologies*, Vol. 238, Springer, 2010.

- [17] D. Thomas, The development of design rules for selective laser melting, Ph.D. thesis, University of Wales (2009).
- [18] D. Brackett, I. Ashcroft, R. Hague, Topology optimization for additive manufacturing, in: Proceedings of the Solid Freeform Fabrication Symposium, Austin, TX, 2011, pp. 348–362.
- [19] M. Leary, L. Merli, F. Torti, M. Mazur, M. Brandt, Optimal topology for additive manufacture: a method for enabling additive manufacture of support-free optimal structures, *Materials & Design* 63 (2014) 678–690.
- [20] A. T. Gaynor, J. K. Guest, Topology optimization for additive manufacturing: considering maximum overhang constraint, in: 15th AIAA/ISSMO multidisciplinary analysis and optimization conference, 2014, pp. 16–20.
- [21] A. T. Gaynor, J. K. Guest, Topology optimization considering overhang constraints: Eliminating sacrificial support material in additive manufacturing through design, *Structural and Multidisciplinary Optimization* 54 (5) (2016) 1157–1172.
- [22] M. Langelaar, An additive manufacturing filter for topology optimization of print-ready designs, *Structural and Multidisciplinary Optimization* (2016) 1–13.
- [23] M. Langelaar, Topology optimization of 3d self-supporting structures for additive manufacturing, *Additive Manufacturing*.
- [24] X. Qian, Undercut and overhang angle control in topology optimization: a density gradient based integral approach, *International Journal for Numerical Methods in Engineering*.
- [25] A. T. Gaynor, J. K. Guest, C. D. Moen, Reinforced concrete force visualization and design using bilinear truss-continuum topology optimization, *Journal of Structural Engineering* 139 (4) (2012) 607–618.
- [26] O. Amir, A topology optimization procedure for reinforced concrete structures, *Computers & Structures* 114 (2013) 46–58.
- [27] J. Norato, B. Bell, D. Tortorelli, A geometry projection method for continuum-based topology optimization with discrete elements, *Computer Methods in Applied Mechanics and Engineering* 293 (2015) 306–327.
- [28] W. Zhang, J. Yuan, J. Zhang, X. Guo, A new topology optimization approach based on moving morphable components (mmc) and the ersatz material model, *Structural and Multidisciplinary Optimization* 53 (6) (2016) 1243–1260.
- [29] M. P. Bendsøe, N. Kikuchi, Generating optimal topologies in structural design using a homogenization method, *Computer methods in applied mechanics and engineering* 71 (2) (1988) 197–224.
- [30] M. P. Bendsøe, Optimal shape design as a material distribution problem, *Structural optimization* 1 (4) (1989) 193–202.
- [31] E. Andreassen, A. Clausen, M. Schevenels, B. S. Lazarov, O. Sigmund, Efficient topology optimization in matlab using 88 lines of code, *Structural and Multidisciplinary Optimization* 43 (1) (2011) 1–16.

- [32] W. S. Dorn, R. E. Gomory, H. J. Greenberg, Automatic design of optimal structures, *Journal de Mecanique* 3 (1964) 25–52.
- [33] P. W. Christensen, A. Klarbring, An introduction to structural optimization, Vol. 153, Springer Science & Business Media, 2008.
- 490 [34] T. Zegard, G. H. Paulino, Grandground structure based topology optimization for arbitrary 2d domains using matlab, *Structural and Multidisciplinary Optimization* 50 (5) (2014) 861–882.
- [35] O. Sigmund, S. Torquato, Design of materials with extreme thermal expansion using a three-phase topology optimization method, *Journal of the Mechanics and Physics of Solids* 45 (6) (1997) 1037–1067.
- [36] B. Bourdin, Filters in topology optimization, *International Journal for Numerical Methods in Engineering* 50 (9) 495 (2001) 2143–2158.
- [37] T. E. Bruns, D. A. Tortorelli, Topology optimization of non-linear elastic structures and compliant mechanisms, *Computer Methods in Applied Mechanics and Engineering* 190 (26) (2001) 3443–3459.
- [38] J. K. Guest, J. H. Prévost, T. Belytschko, Achieving minimum length scale in topology optimization using nodal design variables and projection functions, *International journal for numerical methods in engineering* 500 61 (2) (2004) 238–254.
- [39] K. Svanberg, The method of moving asymptotes- a new method for structural optimization, *International journal for numerical methods in engineering* 24 (2) (1987) 359–373.
- [40] A. Driessen, Overhang constraint in topology optimisation for additive manufacturing: a density gradient based approach, Master’s thesis, TU Delft, Delft University of Technology (2016).
- 505 [41] M. Sonka, V. Hlavac, R. Boyle, Image processing, analysis, and machine vision, Cengage Learning, 2014.
- [42] MATLAB, MATLAB version 9.0.0.341360 (R2016a), The MathWorks, Natick, Massachusetts, 2016.
- [43] O. Amir, N. Aage, B. S. Lazarov, On multigrid-cg for efficient topology optimization, *Structural and Multidisciplinary Optimization* 49 (5) (2014) 815–829.